

Impact of Point Spread Function on Infrared Radiances From Geostationary Satellites

Peng Zhang, Jun Li, Erik Olson, Timothy J. Schmit, Jinlong Li, and W. Paul Menzel

Abstract—The blurring from diffraction for the infrared (IR) radiances on a geostationary satellite (GEO) e.g., the next generation of Geostationary Operational Environmental Satellite (GOES-R) was simulated by using Moderate Resolution Imaging Spectroradiometer Airborne Simulator data and the point spread function (PSF) model for an unobscured telescope. The portion of the total radiance contributed from each nearby geometrical field of view (GFOV) was calculated. For 90% ensquared energy (EE) (equivalent to 10% of the energy coming from outside the footprint), the closest GFOVs contribute 7%; the contribution from the closest GFOVs increases to 22% for 70% EE. The increased portion from the nearby GFOVs causes larger blurring and degrades the pixel-based retrieval product accuracy. Radiance contamination from the nearby field for the GEO IR radiances with 90%, 80%, and 70% EE causes 0.2-, 0.3-, and 0.4-K blurring errors, respectively, in the 12- μm IR longwave window band in clear 300-K scenes. The blurring error is doubled in cloudy 230-K scenes. For the 13.8- μm absorption band, the blurring error will be smaller than that of the 12- μm band because the atmospheric layer where the temperature sensitivity peaks for the 13.8 μm is more uniform than the surface where the 12 μm is most sensitive. This indicates that the PSF has a greater impact on a heterogeneous surface. Similar blurring errors occur at both 4- and 10-km spatial resolution IR sensors. The blurring error is not random, and it varies spectrally. These conclusions are very relevant to the design of a cost-effective GEO IR sounder that meets the science requirements.

Index Terms—Ensquared energy (EE), geostationary satellite (GEO), infrared (IR) radiances, point spread function (PSF).

I. INTRODUCTION

THE PIXEL is used here to describe the elementary unit observed by satellite sensors. For an ideal instrument, the detector output is proportional to the pixel radiance within

the footprint, i.e., the geometrical field of view (GFOV); the information content originates solely from its GFOV. However, real instruments do not exactly reproduce the spatial radiance field of the pixel; a nontrivial portion of the energy comes from the surrounding areas [1], [2]. This energy from outside the GFOV introduces the blurring influence, which degrades the image quality and the pixel-based retrieval product accuracy [3], [4].

Diffraction is one of the unavoidable factors that generate a blurring influence. Diffraction in a satellite sensor occurs because the diameter of the optical system has a limited size. It reduces the detector response from the radiances within the GFOV and increases its response from the radiances outside the GFOV. Other factors, such as the time response of the detector, electronics (analog-to-digital conversion), scan pattern, atmospheric effects, as well as image resampling can cause additional blurring influence [5]. The blurring influence becomes an inherent source of uncertainty in a satellite image. In the study of architectural trades for the satellite sensors, a blurring influence is described by a point spread function (PSF), and the magnitude of the blurring influence is scaled by ensquared energy (EE) [6]. Because of the high orbital altitude, an instrument on a geostationary satellite (GEO) has a larger blurring. To mitigate the blurring influence, high EE is required [7].

High EE is desirable for a pixel-based retrieval product, but it increases the instrument's cost and technical difficulty. A compromise is necessary. This paper provides information to assist in achieving an effective yet scientifically useful GEO infrared (IR) sensor design. The radiances from GEO were simulated for two IR bands and two spatial resolutions with a selected PSF model applied to high spatial resolution airborne measurements. The total radiance and the ratio of radiances from the nearby and far fields were calculated. The brightness temperature difference (BTD) between 100% EE and a given PSF model was quantified. By comparing the BTD with the noise-equivalent TD ($\text{NE}\Delta\text{T}$) required to generate temperature and moisture-profile retrieval, the impact on vertical temperature and moisture soundings was assessed. To generate realistic scenes, Moderate Resolution Imaging Spectroradiometer (MODIS) Airborne Simulator (MAS) data were utilized in the simulation. One clear granule and one cloudy granule were selected to represent a general case and a more heterogeneous case, respectively. IR bands were simulated at 4- and 10-km spatial resolution to represent Geostationary Operational Environmental Satellite (GOES-R) Hyperspectral Environmental Suite (HES) severe weather/mesoscale (SW/M) mode and disk sounding (DS) mode, respectively. The two spectral regions selected are the 12- μm window band and the 13.8- μm CO_2

Manuscript received September 1, 2005; revised December 1, 2005. This work was supported in part by the National Oceanic and Atmospheric Administration (NOAA) under Contract NA07EC0676 relating to the NOAA Advanced Baseline Imager/Hyperspectral Environmental Suite instrument study and in part by the Ministry of Science and Technology of China through the National Basic Research Project 2001CB309402. The views, opinions, and findings contained in this report are those of the authors and should not be construed as an official National Oceanic and Atmospheric Administration or U.S. Government position, policy, or decision.

P. Zhang was with the Cooperative Institute for Meteorological Satellite Studies, University of Wisconsin at Madison, Madison, WI 53706 USA. He is now with the Key Laboratory of Radiometric Calibration and Validation for Environmental Studies, Chinese Meteorological Administration, Beijing 100081, China (e-mail: zhangp@nsmc.cma.gov.cn).

J. Li, E. Olson, and J. Li are with the Cooperative Institute for Meteorological Satellite Studies, University of Wisconsin at Madison, Madison, WI 53706 USA.

T. J. Schmit and W. P. Menzel are with the Office of Research and Applications, National Environmental Satellite, Data, and Information Service, National Oceanic and Atmospheric Administration, Madison, WI 53706 USA.

Digital Object Identifier 10.1109/TGRS.2006.872096

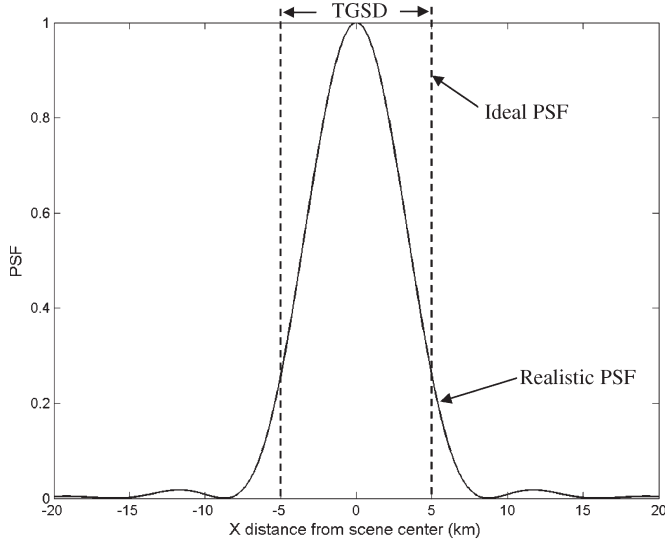


Fig. 1. Realistic and ideal PSF model for simulating GEO radiances.

absorption band. The PSF model is representative for an unobscured telescope.

Section II introduces the PSF and EE used in this paper. Section III describes the data from MAS measurements and the simulation of GEO footprints. Section IV quantifies the portion of the radiance contributed from each set of nearby GFOVs. Section V presents the blurring influence realized for 70%, 80%, and 90% EE. Section VI gives the retrieval results due to the blurring. The conclusions are summarized in Section VII.

II. PSF AND EE

A. PSF Model

The PSF of a sensor describes the response of the sensor to a pencil ray of radiance from a given direction. Therefore, the radiance I measured by the sensor is given by

$$I = \int_{-\infty}^{\infty} dx \int_{-\infty}^{\infty} \text{PSF}(x, y) I_s(x, y) dy \quad (1)$$

where I_s is the scene radiance distributed in the object space, and x and y are scene positions that originated from the peak of the PSF in the object plane. Since I must equal I_s when the scene is uniform, the $\text{PSF}(x, y)$ must satisfy the normalization condition

$$\int_{-\infty}^{\infty} \int_{-\infty}^{\infty} \text{PSF}(x, y) dx dy = 1. \quad (2)$$

In this paper, we utilized an optical PSF model from an unobscured telescope as the realistic model and a rectangle as the ideal model (Fig. 1). The actual shape of the satellite sensor's PSF may differ from (3) because of nonuniform detector response, electronic output noise, and atmospheric scattering.

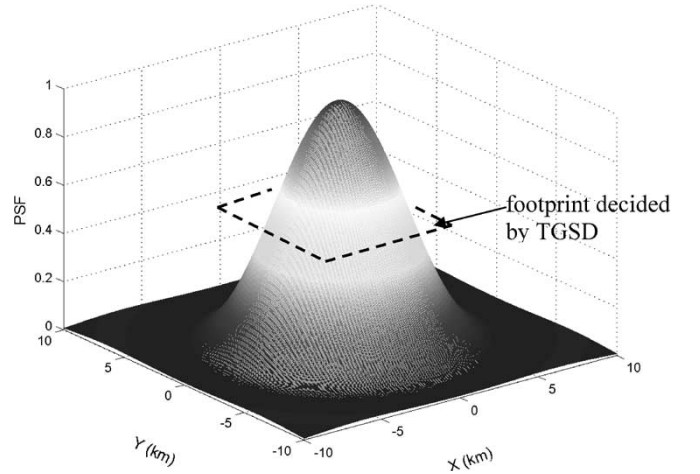


Fig. 2. Sketch of EE in terms of the PSF. Dashed square shows the integral area for EE, which is determined by the TGSD.

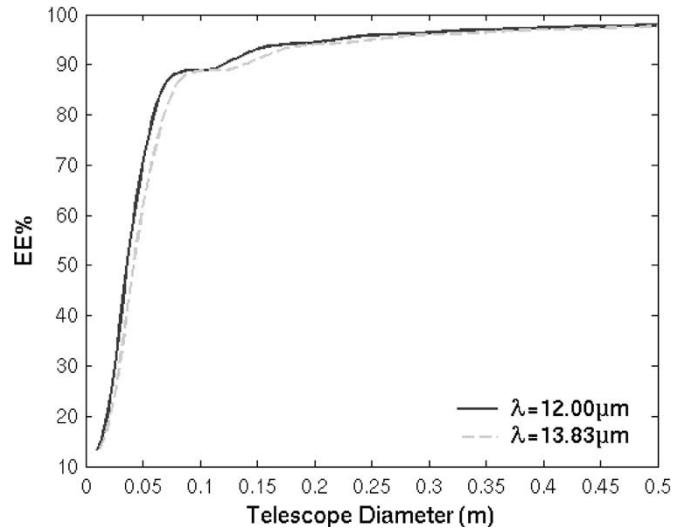


Fig. 3. EE as a function of the telescope diameter for the PSF model in (3).

The optical PSF in object space (i.e., in GEO-coordinate) for a diffraction-limited unobscured telescope is given by [8]

$$\text{PSF}(x, y; \lambda, d, h) = \left[\frac{2J_1 \left(1, \frac{\pi \sqrt{x^2 + y^2}}{\lambda h/d} \right)}{\frac{\pi \sqrt{x^2 + y^2}}{\lambda h/d}} \right]^2 \quad (3)$$

where J_1 is the first-order Bessel function, λ is the wavelength, d is the telescope diameter, and h is the distance from the object. For the GEO measurements, h is the nominal orbital height assumed to be 35 786 km.

The ideal PSF model is given by

$$\text{PSF}(x, y) = \begin{cases} 1, & \leq \text{TGSD} \\ 0, & > \text{TGSD} \end{cases} \quad (4)$$

where TGSD is the threshold ground sample distance, which is the centroid-to-centroid distance between adjacent spatial samples on the Earth's surface as measured at the satellite subpoint.

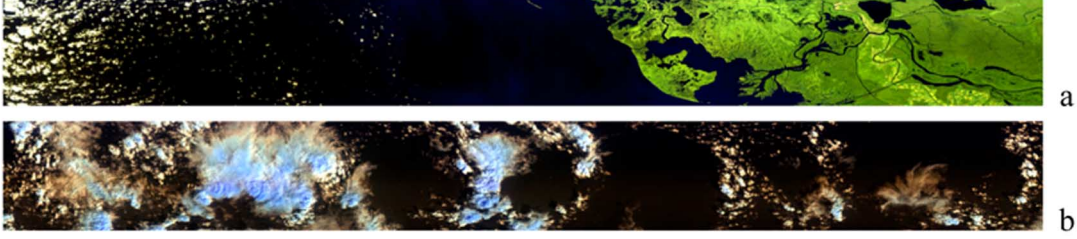


Fig. 4. Red-green-blue composite images of two selected MAS granules. Red with MAS band 20 ($2.15 \mu\text{m}$), green with band 10 ($1.64 \mu\text{m}$), and blue with band 2 ($0.55 \mu\text{m}$). (a) Clear granule from the Terra-Aqua eXperiment 2002 around the Gulf of Mexico and (b) cloudy granule from the THORpex Field Campaign 2003 in the Pacific Ocean around Hawaii.

B. Ensquared Energy

EE, a unitless figure-of-merit, is the ratio of energy detected from the nominal GFOV divided by the energy detected from all GFOVs. According to the HES product and operation requirements document (PORD) [7], the nominal GFOV corresponds to the ground sample area (defined by the TGSD, not the detector active-area projection on the ground). EE can be understood in terms of the PSF (see Fig. 2) as follows:

$$EE = \frac{\int_{-\frac{TGSD}{2}}^{\frac{TGSD}{2}} \int_{-\frac{TGSD}{2}}^{\frac{TGSD}{2}} PSF(x, y) dx dy}{\int_{-\infty}^{\infty} \int_{-\infty}^{\infty} PSF(x, y) dx dy}. \quad (5)$$

As a standard, EE is always referenced to the TGSD. Obviously, the EE of the ideal PSF model in (4) is 100%.

In this paper, only the optical part (diffraction) of the PSF was considered. However, both optical and electrical crosstalk are present in actual detectors. This adds to the wings of the detector spatial response and degrades the EE. With such an EE requirement, the important question is what the impact of the radiances farther away will be, especially in the vicinity of clouds. In a heterogeneous scene, the radiances might be contaminated by fields farther away, and thus, the single-pixel science products will be impacted.

EE in terms of the PSF is the fundamental parameter for measuring the blurring influence. It has been shown that judicious selection of the field-stop shape and its size relative to the sampling pattern can considerably increase the EE and reduce the blurring influence [6]. Fig. 3 shows the increased EE as the function of telescope diameter for the PSF model in (3). The field-stop shape effect on the EE is not covered in this study.

III. DATA AND STUDY AREA

A. MAS Data Selection

In order to simulate the impact of distant fields on the GEO IR radiances, very high spatial resolution data with wide spatial coverage are necessary. The MAS is an airborne scanning spectrometer with 50 channels that measure the reflected solar and thermal emitted radiation from the shortwave visible ($0.5 \mu\text{m}$) through the longwave IR ($14 \mu\text{m}$). It acquires high spatial resolution imagery of cloud and surface features from its vantage point onboard a NASA ER-2 high-altitude research aircraft. The spectrometer is mated to a scanner subassembly, which collects image data with an instantaneous field of view (IFOV) of 2.5 mrad, giving a ground resolution of 50 m from

an altitude of 20 000 m. The swath width of the image is 37.25 km [9]. With such a high spatial resolution, MAS data are ideal for simulating the GEO radiances at several IR spectral regions. The spatial resolution for a GEO IR sounder is usually on the order of 4 to 10 km.

A cloudy and a clear granule were selected from MAS field campaigns (Fig. 4). The clear granule was taken from the Terra-Aqua eXperiment 2002 around the Gulf of Mexico (<http://cimss.ssec.wisc.edu/tx2002>). The cloudy granule was taken from the THORpex Field Campaign 2003 over the Pacific Ocean near Hawaii (http://mas.arc.nasa.gov/data/deploy_html/thorpex_home.html). In Fig. 4(a), the whole scene is very clear except some broken clouds in the upper left part of the image; it represents a very general case of ocean and land surface observed by the satellite. In Fig. 4(b), almost half of the scene is covered by the multilayer clouds; it represents a more heterogeneous case observed by the satellite.

B. Simulation of GEO Footprints

A granule of MAS data contains 37.25 km in the cross-track direction and over 300 km (depending on the distance of the flight route) in the flight-track direction. Because of the narrow swath width, the MAS data were folded in the line direction (up and down) to generate an image that is three times the width (swath) of the original image in order to accurately evaluate the far-field effect of the EE. Fig. 5 shows the folded 12.00- and 13.83- μm BT images for the clear case and cloudy case in Fig. 4.

IV. SIMULATED RADIANCES OF GEO IR SOUNDER

With folded data, the total radiance of GEO measurements at the center footprint can be simulated as follows:

$$I_{\text{GEO}} = \sum_{-(7+\frac{1}{2})TGSD}^{(7+\frac{1}{2})TGSD} \Delta y \sum_{-(7+\frac{1}{2})TGSD}^{(7+\frac{1}{2})TGSD} PSF(x, y) I_{\text{MAS}}(x, y) \Delta x. \quad (6)$$

Seven TGSDs approximate the contribution of the far field. The dashed square areas in Fig. 5 indicate the data surrounded by at least seven TGSDs in all directions.

The total radiance in (6) is the summation of the radiances contributed from the footprint and its surrounding area. Therefore, the individual radiances from the center GFOV

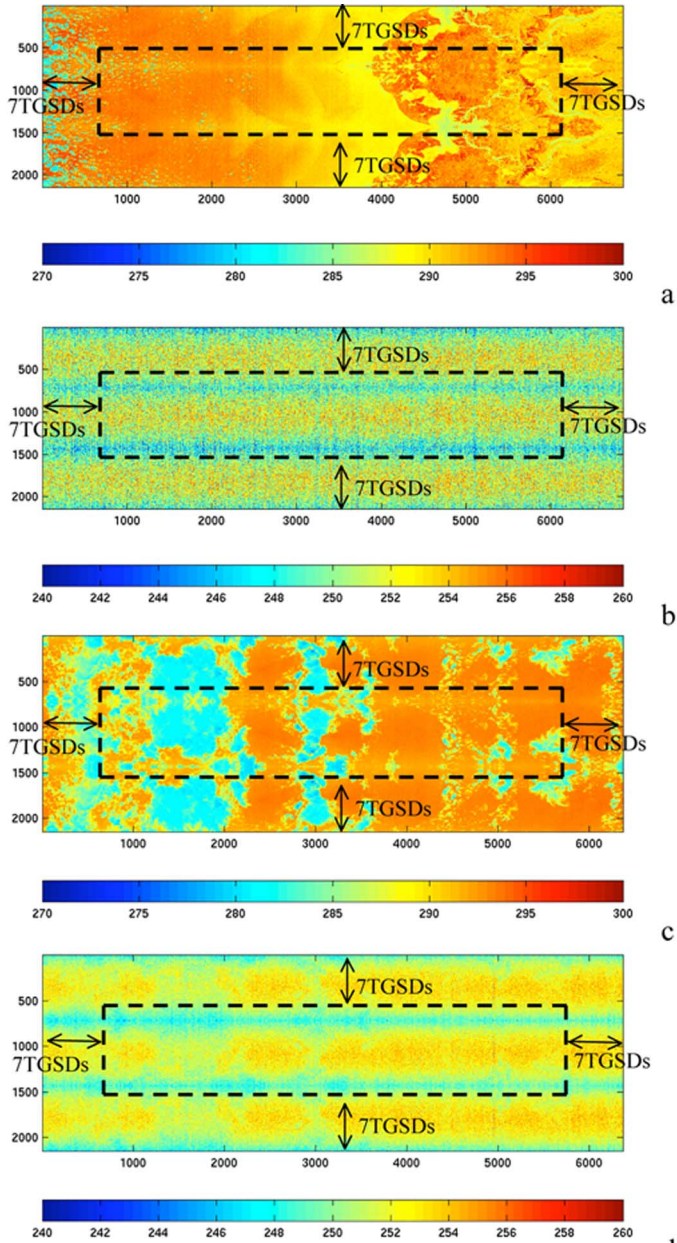


Fig. 5. MAS folded data and area selected for simulated GEO footprints. The abscissa is the MAS scan line number, and the ordinate is the MAS pixel number after folding. The dashed-square areas indicate the data surrounded by at least seven TGSDs in all directions. (a) MAS folded clear scene in BT of 12.00 μm , (b) MAS folded clear scene in BT of 13.83 μm , (c) MAS folded cloudy scene in BT of 12.00 μm , and (d) MAS folded cloudy scene in BT of 13.83 μm . Double arrows show seven TGSDs around the footprints for EE simulation.

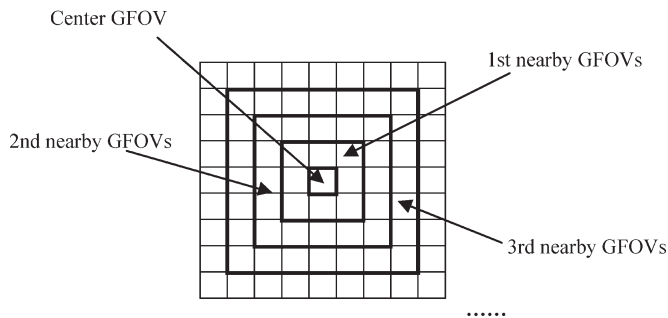


Fig. 6. Diagram of the nearby GFOVs.

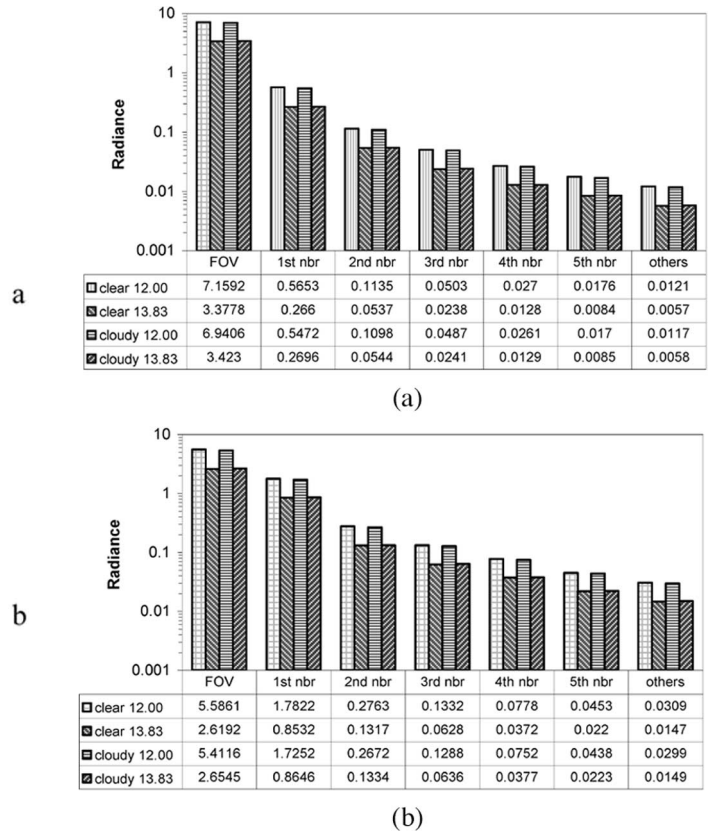


Fig. 7. Averaged radiance contributed from each individual component. The radiance of individual components computed from (7) and (8). Four bars show the results for the clear scene and cloudy scene at 12.00 and 13.83 μm , respectively. Corresponding values are given also at the bottom table of the figure. The unit of the radiance is watts per square meter per steradian per micron). All the values were averaged within the selected area indicated in Fig. 5: (a) 90% EE and (b) 70% EE.

(footprint), the first nearby GFOV, the second nearby GFOV, etc., are given by

$$I_{\text{GEO}}^0 = \sum_{-\frac{\text{TGSD}}{2}}^{\frac{\text{TGSD}}{2}} \Delta y \sum_{-\frac{\text{TGSD}}{2}}^{\frac{\text{TGSD}}{2}} \text{PSF}(x, y) I_{\text{MAS}}(x, y) \Delta x \quad (7)$$

$$I_{\text{GEO}}^i = \sum_{-(i+\frac{1}{2})\text{TGSD}}^{(i+\frac{1}{2})\text{TGSD}} \Delta y \sum_{-(i+\frac{1}{2})\text{TGSD}}^{(i+\frac{1}{2})\text{TGSD}} \text{PSF}(x, y) I_{\text{MAS}}(x, y) \Delta x - \sum_{-(i-\frac{1}{2})\text{TGSD}}^{(i-\frac{1}{2})\text{TGSD}} \Delta y \sum_{-(i-\frac{1}{2})\text{TGSD}}^{(i-\frac{1}{2})\text{TGSD}} \text{PSF}(x, y) I_{\text{MAS}}(x, y) \Delta x \quad (8)$$

where I_{GEO}^0 means the radiance from the center GFOV, and I_{GEO}^i means the radiance from the i th nearby GFOV for $i \geq 1$. Fig. 6 shows a sketch of surrounding nearby GFOVs. The square is assumed for each footprint in the simulation as an approximation.

Fig. 7(a) shows the averaged radiance from each individual component for 90% EE while Fig. 7(b) is the same for 70%. Table I shows the averaged ratio of each individual component to the total radiance. All the values in Fig. 6 and Table I were averaged within the selected area indicated in Fig. 5.

TABLE I
AVERAGED RATIO OF EACH COMPONENT I_{GEO}^i TO THE TOTAL RADIANCE

Case	Percentage (%)													
	Center FOV		1st nbr		2nd nbr		3rd nbr		4th nbr		5th nbr		others	
	90%	70%	90%	70%	90%	70%	90%	70%	90%	70%	90%	70%	90%	70%
	EE	EE	EE	EE	EE	EE	EE	EE	EE	EE	EE	EE	EE	EE
Clear 12.00	90.11	70.43	7.12	22.47	1.43	3.48	0.63	1.68	0.34	0.98	0.22	0.57	0.15	0.39
Clear 13.83	90.12	70.02	7.10	22.81	1.43	3.52	0.63	1.68	0.34	0.99	0.22	0.59	0.15	0.39
Cloudy 12.00	90.12	70.45	7.11	22.46	1.43	3.48	0.63	1.68	0.34	0.98	0.22	0.57	0.15	0.39
Cloudy 13.83	90.12	70.02	7.10	22.81	1.43	3.52	0.63	1.68	0.34	0.99	0.22	0.59	0.15	0.39

For the 90% EE, 10% of the radiances are from pixels outside the center pixel of which 7% comes from the first set of adjacent pixels (first nearby GFOVs), 1.4% (second), 0.6% (third), 0.3% (4th), 0.2% (5th), and 0.5% comes from pixels outside of the fifth nearby GFOVs. For the 70% EE, the contributions from the first nearby GFOVs increase rapidly up to 22%. The contributions from other nearby GFOVs have also increased.

At the absorption band (e.g., 13.8 μm), the blurring influence from the nearby GFOVs tends to be less than at the window band due to the fact that 13.83- μm scene tends to be more homogeneous. The results of a GEO IR sounder with 4-km resolution are similar to those of a GEO IR sounder with 10-km resolution. However, in some extreme footprints (uniform scene), the nearby field impact can be larger than that of a GEO with a 10-km resolution.

V. NEARBY AND FAR-FIELD GFOVs' INFLUENCE ON BT

It is very important to quantify the influence on the measured radiance from the nearby and far-field GFOVs for a specific EE. Here, we define the blurring influence as the BTD between the BT simulated with a specific EE and the BT simulated with the ideal PSF (100% EE) defined by (4). BT can be derived from the simulated radiance with the inversion of the Planck function as follows:

$$\text{BT} = \frac{C_2}{\lambda \ln \left(\frac{C_1}{\pi I_{\text{GEO}} \lambda^5} + 1 \right)} \quad (9)$$

where C_1 is the first radiation constant and $C_1 = 3.7418 \times 10^{16} \text{ W/m}^2$. C_2 is the second radiation constant and $C_2 = 1.43879 \times 10^2 \text{ m} \cdot \text{K}$.

Fig. 8 and Table II show the calculated blurring influence for the two simulated IR sensor spatial resolutions (10 km for HES DS and 4 km for HES SW/M on GOES-R) in the clear scene and cloudy scene at 12.00 and 13.83 μm , respectively. The simulated footprint contains 200×200 MAS pixels for 10-km spatial resolution and 80×80 for 4-km spatial resolution. The calculations show that in clear skies, for a GEO IR sounder with 10-km resolution, 90%, 80%, and 70% EE can result in blurring influence up to 0.2, 0.3, and 0.4 K, respectively, with IR longwave window band (e.g., 12 μm). While in cloudy skies, the influence is amplified up to 0.4, 0.6, and 0.8 K, respectively.

VI. IMPACT OF BLURRING ON TEMPERATURE AND MOISTURE RETRIEVAL

The impact of blurring on retrieval has been studied using MODIS 1-km IR data. HES footprints with 10-km spatial resolution are simulated at 11 MODIS IR spectral bands with 100% EE, 90% EE, 80% EE, and 70% EE. Fig. 9 shows the BTD between 100% EE and 90%, 80%, 70% EE, respectively, for the MODIS 11 IR spectral bands. MODIS granule data at 1915 universal time coordinate (UTC) on September 6, 2002 is used. Only clear simulated footprints with 10-km spatial resolution are included in the retrieval test. It can be seen that the blurring BTD is not random; it varies spectrally. The BTD is larger in the window bands than those in the absorption bands. The BTD impact on temperature and moisture retrieval can be quantified with MODIS IR data. Temperature and moisture profiles were retrieved using the 11 MODIS IR bands at 10-km footprint size with an operational algorithm [10]. The root mean square error temperature and moisture retrieval due to 90% EE, 80% EE, and 70% EE are computed by the assumption that 100% EE is true. The root mean square error here represents the blurring impact on sounding retrieval. Fig. 10 shows the temperature (left panel) and relative humidity (RH) (right panel) additional retrieval error due to 90%, 80%, and 70% EE. It can be seen that 90%, 80%, and 70% EE will cause approximately 0.07-, 0.10-, and 0.15-K additional temperature retrieval errors, respectively, in boundary layer with MODIS. For the water-vapor RH, 90%, 80%, and 70% EE will cause approximately

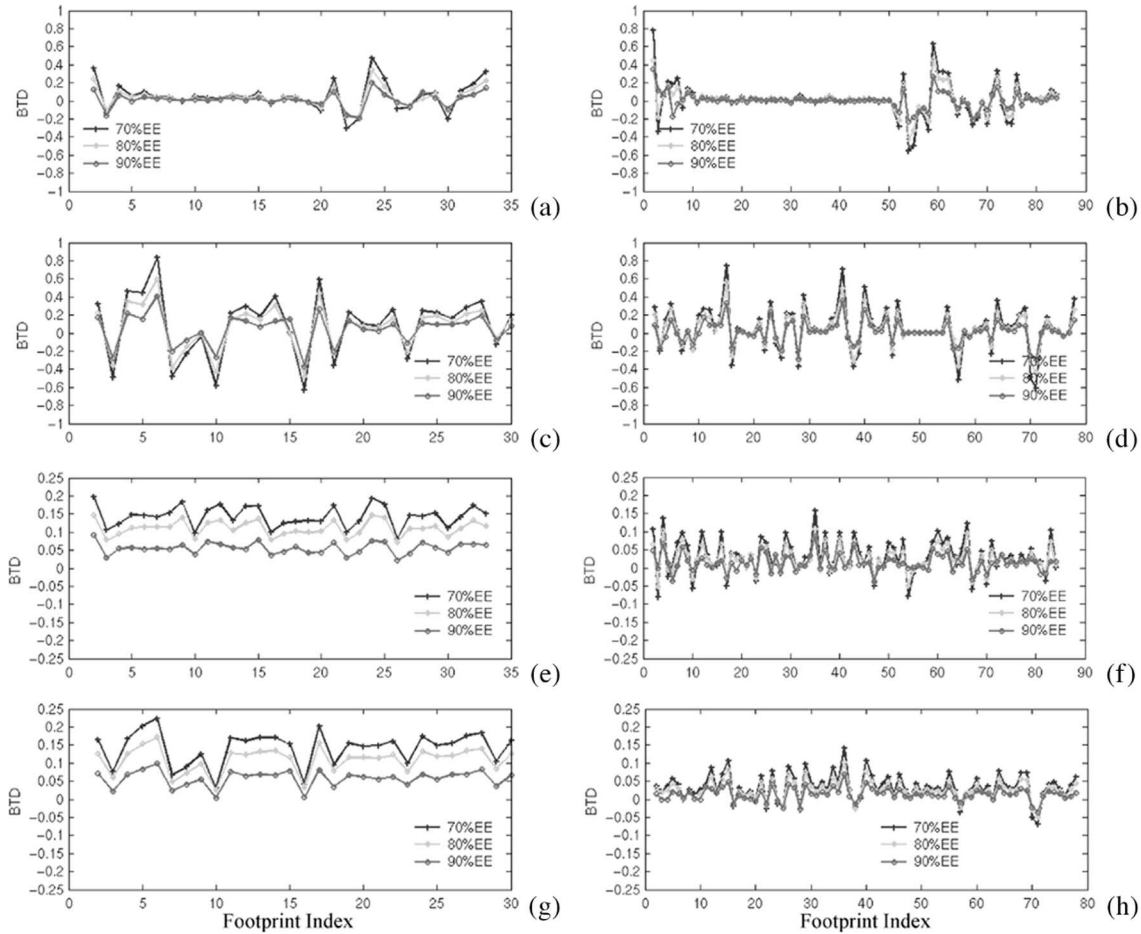


Fig. 8. Blurring influence of the radiance from the nearby and far field. The abscissa shows the simulated footprint index (the first footprint, the second, the third, . . .) along the center line in Fig. 5, and the ordinate shows the blurring influence in BTD: (a) clear 10 km 12.0 μm , (b) clear 4 km 12.0 μm , (c) cloudy 10 km 12.0 μm , (d) cloudy 4 km 12.0 μm , (e) clear 10 km 13.8 μm , (f) clear 4 km 13.8 μm , (g) cloudy 10 km 13.8 μm , and (h) cloudy 4 km 13.8 μm .

TABLE II
MAXIMUM BTD AND RMS BTD IN FIG. 7

Case	BTD (K)					
	90% EE		80% EE		70% EE	
	Max	RMS	Max	RMS	Max	RMS
clear, 10km, 12.00 μm	0.20	0.08	0.34	0.11	0.47	0.17
cloudy, 10km, 12.00 μm	0.41	0.18	0.59	0.27	0.84	0.37
clear, 4km, 12.00 μm	0.35	0.09	0.46	0.13	0.78	0.19
cloudy, 4km, 12.00 μm	0.36	0.12	0.55	0.18	0.75	0.25
clear, 10km, 13.83 μm	0.09	0.06	0.15	0.11	0.20	0.15
cloudy, 10km, 13.83 μm	0.10	0.06	0.17	0.11	0.22	0.15
clear, 4km, 13.83 μm	0.09	0.03	0.11	0.04	0.16	0.06
cloudy, 4km, 13.83 μm	0.07	0.02	0.10	0.04	0.14	0.05

0.4%, 0.6% and 0.8% additional retrieval errors, respectively. It should be noted that the results are from MODIS, which is low spectral resolution. The impact on retrieval with high spectral resolution IR data might be different.

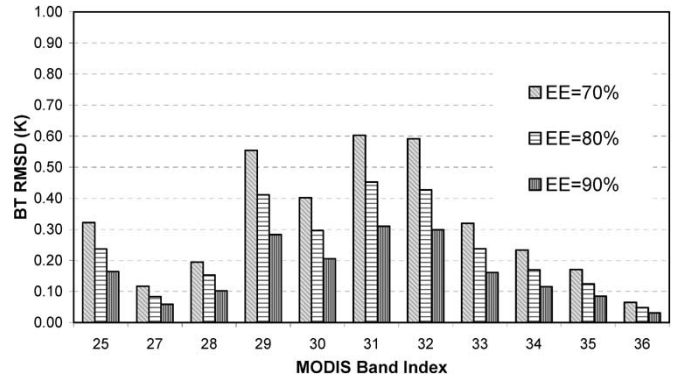


Fig. 9. BTD between 100% EE and 70%, 80%, 90% EE, respectively, for the MODIS 11 IR spectral bands.

VII. CONCLUSION

In this paper, the blurring influences on IR radiances measured from GEO orbit were simulated using MAS data and the PSF model from an unobscured telescope. From the calculations, we can see the following.

- 1) Effect of the EE value dominates the portion of radiance contributed from the nearby and far fields. For the 90% EE case, 7% are contributed from the first nearby GFOVs

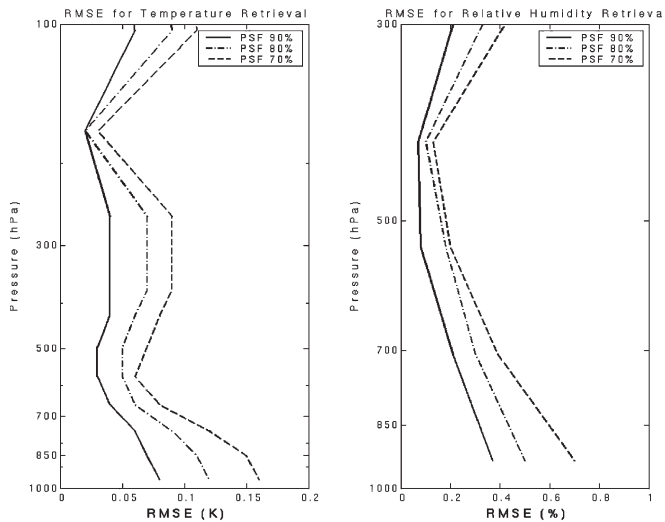


Fig. 10. (Left) Temperature and (right) RH additional retrieval error due to 90%, 80%, and 70% EE, respectively.

while the contribution from the first nearby GFOVs increases up to 22% for the 70% EE case.

- 2) Blurring influences from the nearby and far fields have been quantified. The GEO radiances with 90%, 80%, and 70% EE will cause approximately 0.2-, 0.3-, and 0.4-K differences from 100% EE at 12.00- μm IR longwave window band in the clear scenes. The blurring influence is doubled in the cloudy scenes. In the 13.83- μm absorption region, the corresponding blurring influence will be smaller than that in the 12.00- μm band because the layer at which the temperature-sensitivity peaks for 13.83- μm tend to sense a more uniform scene than at the surface. The PSF has a greater impact on the heterogeneous surface. Similar blurring influence is seen in both the 4- and 10-km resolution IR sounder simulations, except in the vicinity of a few unusually hot or cold pixels.
- 3) Blurring error is not random, it varies spectrally.

If the PSF is well known, some of the blurring might be mitigated, which worth a further study. The prelaunched characterization of the PSF is important to estimate the impact of the blurring.

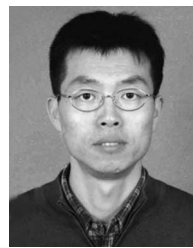
ACKNOWLEDGMENT

The authors would like to thank the Cooperative Institute for Meteorological Satellite Studies colleagues for their cooperation in this study.

REFERENCES

- [1] J. R. G. Townshend, "The spatial resolving power of Earth resources satellite," *Prog. Phys. Geogr.*, vol. 5, no. 1, pp. 32–55, 1981.
- [2] B. L. Markham, "The Landsat sensors spatial responses," *IEEE Trans. Geosci. Remote Sens.*, vol. GRS-23, no. 6, pp. 864–875, Nov. 1985.
- [3] F. O. Huck, N. Halyo, and S. K. Park, "Aliasing and blurring in 2-D sampled imagery," *Appl. Opt.*, vol. 19, no. 13, pp. 2174–2181, Jul. 1980.
- [4] C. Huang, J. R. G. Townshend, S. Liang, S. N. V. Kalluri, and R. S. DeFries, "Impact of sensor's point spread function on land cover characterization: Assessment and deconvolution," *Remote Sens. Environ.*, vol. 80, no. 2, pp. 203–212, May 2002.
- [5] G. L. Smith, "Effects of time response on the point spread function of a scanning radiometer," *Appl. Opt.*, vol. 33, no. 30, pp. 7031–7037, Oct. 1994.

- [6] M. E. MacDonald, E. C. Wack, M. W. Kelly, D. P. Ryan-Howard, M. M. Coakley, D. M. Weitz, H. R. Finkle, D. E. Weidler, G. W. Carlisle, and L. M. Candell, "Architectural trades for an advanced geostationary atmospheric sounding instrument," in *Proc. IEEE Aerosp. Conf.*, 2001, vol. 4, pp. 1693–1711.
- [7] Goddard Space Flight Center, GOES Hyperspectral Environmental Suite (HES) Performance and Operation Requirements Document (PORD), pp. 51–60, NOAA technical documents: 417-R-HESPORD-0020, 2003.
- [8] M. Born and E. Wolf, *Principles of Optics, Electromagnetic Theory of Propagation Interference and Diffraction of Light*, 6th ed. New York: Pergamon, 1980.
- [9] M. D. King, W. P. Menzel, P. S. Grant, J. S. Myers, G. T. Arnold, S. E. Platnick, L. E. Gumley, S. C. Tsay, C. C. Moeller, M. Fitzgerald, K. S. Brown, and F. G. Osterwisch, "Airborne scanning spectrometer for remote sensing of cloud, aerosol, water vapor and surface properties," *J. Atmos. Ocean. Technol.*, vol. 13, no. 4, pp. 777–794, 1996.
- [10] S. W. Seemann, J. Li, W. P. Menzel, and L. E. Gumley, "Operational retrieval of atmospheric temperature, moisture, and ozone from MODIS infrared radiances," *J. Appl. Meteorol.*, vol. 42, no. 8, pp. 1072–1091, 2003.



Peng Zhang received the M.S. degree in atmospheric optics from the Anhui Institute of Optics and Fine Mechanics, Chinese Academy of Sciences (AIOFM/CAS), Anhui, in 1995, and the Ph.D. degree in atmospheric physics, in which his work focused on the algorithm study to retrieve the physical and optical properties of aerosols by using the reflected solar radiance from satellite measurements, from the Institute of Atmospheric Physics (IAP), CAS, Beijing, in 1998.

From 1998 to 2001, he spent over three years in the Earth Observation Research Center, National Space Development Agency of Japan with a Postdoctoral position to integrate and implement the standard atmospheric retrieval algorithm for the Global Land Imager sensor and the ADEOS II satellite. Since 2001, he has been working in the National Satellite Meteorological Center, China Meteorological Administration, as an Associate Professor, from November 2001 to November 2005, and a Professor from December 2005 up to the present. He was a Visiting Scholar at the Centre de Meteorologie Spatiale, Meteo-France from September 2003 to December 2003. He was a Visiting Associate Scientist at the Cooperative Institute for Meteorological Satellite Studies, Space Science and Engineering Center, University of Wisconsin at Madison from February 2005 to September 2005. Currently, he is the Principle Investigator to design the hyperspectral IR sensor on the Fengyun 3 series (next-generation polar meteorological satellite in China) and Fengyun 4 series (next-generation geostationary meteorological satellite in China). His research interests include atmospheric sounding with high spectral resolution sensors, aerosols retrieval (especially dust-storm retrieval), trace-gases retrieval, and atmospheric radiation transfer calculations.



Jun Li received the B.S. degree in mathematics from Peking University, Beijing, China, in 1987, and the M.S. and Ph.D. degrees in atmospheric science from the Institute of Atmospheric Physics, Chinese Academy of Science, Beijing, in 1990 and 1996, respectively.

In 1997, he joined the Space Science and Engineering Center (SSEC), University of Wisconsin at Madison, where he was responsible for developing the algorithms to retrieve atmospheric and cloud parameters from the Moderate Resolution Imaging Spectrometer, the National Polar Orbiting Environmental Satellite System Airborne Sounder Testbed—Interferometer, and the Atmospheric Infrared Sounder measurements. His research interests include deriving atmospheric temperature and moisture profiles, as well as cloud properties from hyperspectral IR sounder and Multispectral Imager data. He is currently an Associate Scientist with SSEC, and the Principal Investigator of the current Geostationary Operational Environmental Satellite (GOES) Improved Measurement and Product Assurance Plan and the future GOES-R's Hyperspectral Environmental Suite and Advanced Baseline Imager instrument studies at the Cooperative Institute for Meteorological Satellite Studies (CIMSS). He is also a member of GOES-R Algorithm Working Group.



Erik Olson received the B.S. degree in physics from the University of Minnesota-Twin Cities, Minneapolis, and the M.S. degree in atmospheric science from the University of Wisconsin-Madison, Madison, in 1994 and 2000, respectively.

He is currently with the Space Science and Engineering Center, University of Wisconsin-Madison as part of the Cooperative Institute for Meteorological Satellite Studies. His research interests include high spectral infrared observations, which include satellite-, aircraft-, and ground-based instruments,

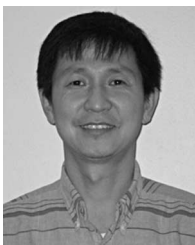
with his projects ranging from processing field data, calibration algorithm development, and simulated observation generation.



Timothy J. Schmit received the M.S. degree in meteorology from the University of Wisconsin-Madison, Madison, in 1987.

He is currently with the Advanced Satellite Products Branch, National Oceanic and Atmospheric Administration, National Environmental Satellite, Data, and Information Service, Office of Research and Applications, Madison, WI. His experience with satellite data and processing covers a number of areas including calibration, simulations, and algorithms for processing satellite data into meteorological

information and has a lead role in some of the science applications for GOES-R. He has worked on deriving Visible and Infrared Spin Scan Radiometer Atmospheric Sounder retrievals/gradient winds from GOES-6/7, simulating the GOES-I (-8) instruments (both imager and sounder), calibration, deriving meteorological products from the current sounder and imager, and helping to prepare for the next-generation geostationary imagers (ABI) and sounders (HES). This work, in preparation for GOES-R, includes working on how requirements could be met, data distribution, calibration, ABI band selection, and simulating both the imager and sounder expected radiance signals via forward modeling and modifying data from existing research satellites.



Jinlong Li received the B.S. degree from the Nanjing Institute of Meteorology, Nanjing, China, and the M.S. degree from the Institute of Atmospheric Physics, Chinese Academy of Sciences, Beijing, in 1985 and 1990, respectively, both in atmospheric dynamics, and the Ph.D. degree in atmospheric sciences from the Georgia Institute of Technology, Atlanta, in 2001.

His research interests include numerical weather forecasts, long-term ozone changes in the stratosphere, and trace-gas-emission estimates. Since he

joined the Cooperative Institute for Meteorological Satellite Studies, Madison, WI, in 2005, his research interests have focused on the development of a new algorithm for the retrieval of current and next-generation GOES products.



W. Paul Menzel received the B.S. degree in physics from the University of Maryland, College Park, and the M.S. and Ph.D. degrees in theoretical solid-state physics from the University of Wisconsin, Madison, in 1967, 1968, and 1974, respectively.

In 1975, he joined the Space Science and Engineering Center, University of Wisconsin, where he was among the first to explore the possibilities for remote sensing of the Earth's atmosphere from a geosynchronous satellite. Specifications for the vertical temperature and moisture sounding capabilities of

the VISSR VAS were the result of that work. In 1983, he joined the National Oceanic and Atmospheric Administration (NOAA), National Environmental Satellite, Data, and Information Service, Madison, WI, to lead the Advanced Satellite Products Project, where he was responsible for the development, testing, and evaluation of procedures for deriving new atmospheric products from spaceborne observations, which focused on transferring advances made in the research laboratory to the operational weather forecaster. His early work focused on calculating the band structure properties of alkali halides using the method of linear combinations of atomic orbitals in a Hartree-Fock formulation. He is currently a Senior Scientist with the NOAA Satellite and Information Services, where he is responsible for conducting and stimulating research on environmental remote sensing systems, fostering expanded utilization of those systems locally and globally, and assisting in the evolution of the NOAA polar orbiting and geostationary satellite holdings. He is also a member of the MODIS Science Team, working on algorithms to derive cloud-top properties, atmospheric profiles, and column water vapor using infrared bands on MODIS. He is the Chair of the World Meteorological Organization (WMO) Expert Team on Evolution of the Global Observing System, which assesses the capabilities of *in situ* plus satellite observing systems for meeting user requirements in several weather and climate application areas. He is also the Science Director of the Cooperative Institute for Meteorological Satellite Studies and an Adjunct Professor in atmospheric and oceanic sciences with the University of Wisconsin. He is the author of a textbook on remote sensing applications with meteorological satellites, which is freely available through the WMO for education and training and is being used internationally in university classrooms and WMO seminars for training the trainers. His research interests include remote sensing of atmospheric temperature and moisture profiles, total column ozone, cloud properties, and surface properties.